Geophysical Journal International

Geophys. J. Int. (2024) **239,** 201–217
Advance Access publication 2024 August 01
GJI Seismology

https://doi.org/10.1093/gji/ggae267

Dynamic evolution of West Gondwana inferred from crustal anisotropy of the South American platform

Mei Feng [1], Meijian An [1], Hulin Zang,[1,†] Marcelo S. Assumpção [2], Marcelo B. Bianchi [2], George S. França,[2] Marcelo P. Rocha,[3] Leda S. Bettucci[4] and Carlos A. Chaves [2]

[1] *Chinese Academy of Geological Sciences, Beijing 100037, China. E-mail: mei_feng_cn@163.com*
[2] *Department of Geophysics, Institute of Astronomy, Geophysics and Atmospheric Sciences, University of São Paulo, São Paulo 05508-090, Brazil*
[3] *Seismological Observatory, Institute of Geosciences, University of Brasília, Brasília 70910-900, Brazil*
[4] *Geophysical Observatory of Uruguay, Faculty of Sciences, University of the Republic, Montevideo 11400, Uruguay*

Accepted 2024 July 30. Received 2024 June 14; in original form 2024 February 7

SUMMARY

The amalgamation and breakup of the West Gondwana shaped the South American platform. The dynamics during the processes can be reflected by crust anisotropy of the platform, but there are no specialized crustal anisotropic measurements yet. Splitting analysis of Moho-converted shear waves in *P*-wave receiver functions (*Pms*) can reveal crustal-scale anisotropy, which is important for understanding the dynamic evolution of the crust and for the interpretation of mantle anisotropy from splitting analysis of core–mantle refracted shear waves (*XKS* phases). This study measured crustal anisotropy for the old and stable South American platform by *Pms* splitting analysis. The splitting times vary mainly in the range of 0–0.5 s, with a regional mean of 0.2 s, slightly lower than that observed in tectonically active regions. The detected crustal anisotropy shows distinct characteristics and spatial zoning, providing insights into tectonic processes. (1) Fast polarization directions at stations close to the Transbrasiliano Lineament (TBL) are oriented NNE–SSW, generally consistent with the strike of the TBL but inconsistent with the maximum horizontal compressive stress, implying that they might be formed by dynamic metamorphism during the formation of the TBL. (2) Crustal anisotropy along the passive continental margin in the east and northeast is weak. Still, the fast polarization directions tend to be oriented along the margin, implying the existence of fossil extensional crustal fabrics formed during the continental rifting of West Gondwana. (3) The Paraná Basin, one of the world's largest Large Igneous Provinces (LIP) covered by continental flood basalts, shows distinctively strong anisotropy, with fast polarization directions highly aligned with mantle anisotropy, implying that synchronous crust–mantle deformation occurred in these regions as a result of magmatism during the breakup of West Gondwana.

Key words: South America; Body waves; Seismic anisotropy; Crustal structure.

1. INTRODUCTION

Cratonic blocks in South America (Fig. 1) and Africa amalgamated and welded by fold belts in Neoproterozoic and finally formed West Gondwana during the Brasiliano-Pan African orogeny (ca. 1000 to 500 Ma; Cordani *et al.* 2000, 2009, 2016a). West Gondwana broke into South America and Africa during the opening of the South Atlantic in the Mesozoic (Cordani *et al.* 2009). The present stable (central and eastern) part of South America, the South American platform, is the part involved in the amalgamation and breakup of West Gondwana (Fig. 1). Seismic anisotropy is a good detector of the dynamics of tectonic events. After the breakup of West Gondwana in the Cretaceous (Cordani *et al.* 2009), the platform has suffered little tectonic deformation making it an ideal place for tracing the ancient imprints of tectonic evolution by seismic anisotropy.

Shear waves passing through anisotropic media split into fast and slow waves (Crampin 1979; Zang *et al.* 2023), which has been widely observed in the upper crust, middle-to-lower crust and mantle. The analysis of shear wave splitting characteristics can extract the parameters of anisotropy (i.e. fast polarization direction φ and

[†] Now at South China Sea Institute of Oceanology, Chinese Academy of Sciences, Guangzhou, China

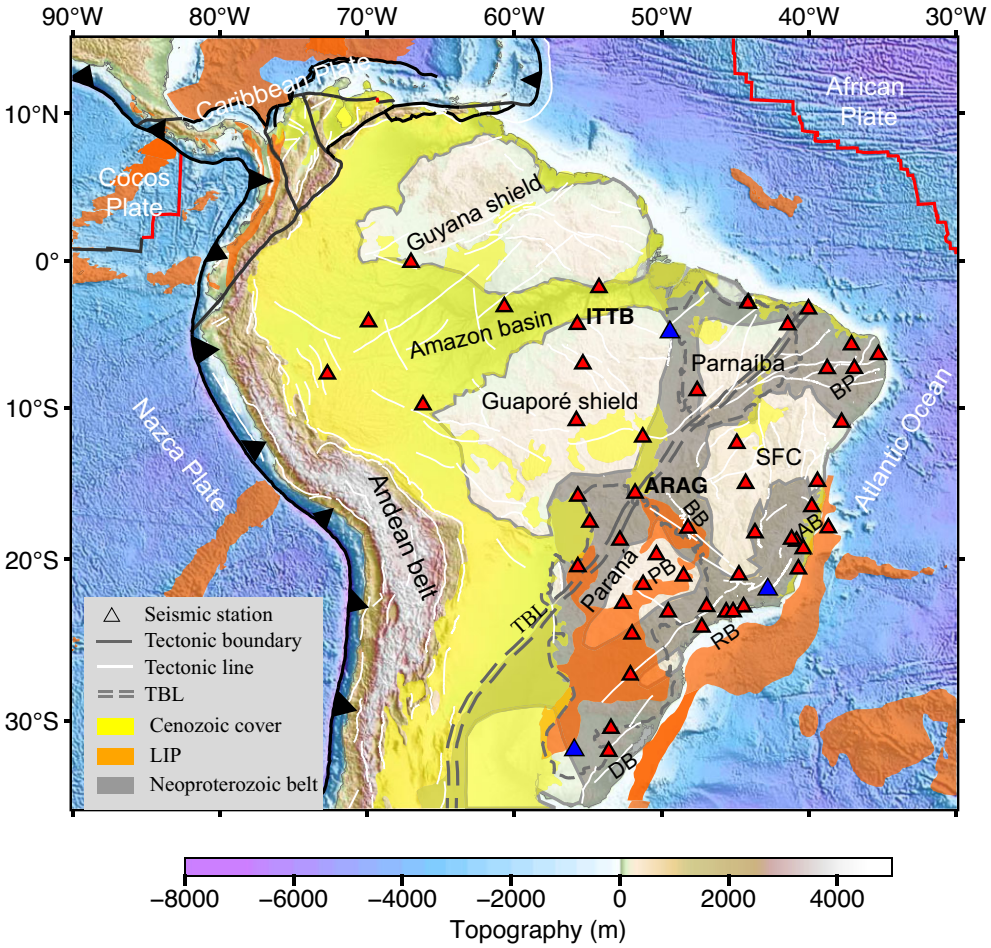

Figure 1. Tectonic setting and configuration of the South American platform (Cordani *et al.* 2009, 2016b). The areas which are not covered by grey and yellow shades in the central and eastern South American are of cratonic blocks. Red and blue triangles are 66 broad-band seismic stations of the RSBR and three newly deployed portable stations, respectively. ITTB and ARAG are two RSBR stations to be further discussed in Figs 3 and 9. Data for LIPs are from Coffin *et al.* (2013). AB = Araçuaí Belt, BB = Brasília Belt, BP = Borborema Province, DB = Dom Feliciano Belt, PB = Paranapanema block, RB = Ribeira Belt, SFC = São Francisco Craton and TBL = Transbrasiliano Lineament.

splitting time τ), which in turn can be used to infer anisotropic structures in the crust and mantle (Crampin 1979; Silver & Chan 1991; Gao *et al.* 2012). Shear waves with different propagation paths can be used to gain information about anisotropic structures down to different depths which may reflect different deformation mechanisms and tectonic processes (Nicolas & Christensen 1987; Liu & Niu 2012).

The splitting of core–mantle refracted shear waves (*XKS* phases) can be used to measure mantle anisotropy if crustal anisotropy is weak or negligible (e.g. Wüstefeld *et al.* 2009; Gao *et al.* 2010; Becker *et al.* 2012; Shi *et al.* 2012). The measurements on seismic anisotropy of the South American platform from *XKS* splitting analysis (Heintz *et al.* 2003; Assumpção *et al.* 2006; Assumpção *et al.* 2011; Chagas de Melo *et al.* 2018) show weak lateral variation in the fast polarization direction in the South American platform with an overall direction in generally E–W. Most of the fast polarization directions of the *XKS* phases are similar to the direction of absolute plate motion relative to the hotspot reference model HS3-NUVEL1A (Gripp & Gordon 2002), implying the dominance of flow-induced deformation in the asthenosphere. However, local-scale lateral variations in fast polarization directions have been observed in the Amazon Craton, Paraná Basin and southern São Francisco Craton (SFC), indicating relict deformation in the thick lithosphere and/or local disturbance of a thick lithospheric root to mantle flow (Assumpção *et al.* 2006; Chagas de Melo *et al.* 2018). These interpretations of *XKS* splitting results are based on the assumption of negligible crustal anisotropy.

An approximate understanding of crustal-scale anisotropy for the South American platform has been given by the global surface wave tomographic model of Debayle *et al.* (2016, Fig. S6 in the Supporting Information). However, the resolution of that surface wave model is insufficient to allow any possible relationship to be established between anisotropy and heterogeneous surface geology (Cordani *et al.* 2000,2009). The splitting of Moho-converted shear waves (*Pms*) can be used to measure anisotropy in the entire crust (crustal-scale or whole-crust anisotropy, e.g. Chen *et al.* 2013; Watanabe & Oda 2015; Licciardi *et al.* 2018). The splitting times of *Pms* data observed in the global crust can be as large as 0.2 s in stable basin regions (e.g. Chen *et al.* 2013) and 0.7 s in seismically active regions (e.g. Nagaya *et al.* 2008), which are not substantially smaller than the global average *XKS* splitting time of ∼1.0 s (Savage 1999), implying that crustal anisotropy is not always negligible when interpreting *XKS* splitting data. Strong crustal anisotropy has been observed in tectonically active regions (e.g. Chen *et al.* 2013; Watanabe & Oda 2015; Licciardi *et al.* 2018) and in the cratonic crust in South Africa (Thybo *et al.* 2019). However, no results have

been obtained for crustal-scale anisotropy from the splitting analysis of *Pms* data for the South American platform.

In this study, we conducted a splitting analysis of *Pms* data recorded by broad-band seismic stations on the South American platform to infer the structure of crustal-scale anisotropy below the stations. Results are then used to assess the sources/causes of the crustal anisotropy, which are likely involved in the evolution of West Gondwana.

2. TECTONICS OF THE SOUTH AMERICAN PLATFORM

The South American platform (Fig. 1) is the old and stable part of the central and eastern South American continent. It is bordered by the Andean orogenic belt to the west and northwest, and by passive continental margins to the east and northeast. The platform includes the Amazon Craton (Guyana and Guaporé shields) in the northwest and the SFC and the cratonic Paraná Basin (one of the world's largest Large Igneous Provinces , LIP, e.g. Sensarma *et al.* 2018) in the southeast. The platform is transected by a large shear zone, the Transbrasiliano (or Trans-Brazilian) Lineament (TBL; Fig. 1) (Cordani *et al.* 2000, 2009).

The South American platform emerged when several continental masses were amalgamated to form West Gondwana during the Brasiliano-Pan African orogenic cycle (ca. 1000 to 500 Ma, Cordani *et al.* 2016a). The Amazonian (Guyana and Guaporé shields, Fig. 1) and the West African cratonic masses collided with the São Francisco-Congo, the Río de La Plata and the Saharan cratonic masses and formed the Brasília and Paraguay orogenic belts, the Borborema tectonic Province (BP), or the Transbrasiliano shear zone (TBL) in South America and the Kandi Shear Zone (KSZ) in Africa. The São Francisco-Congo palaeocontinent amalgamated with some smaller cratonic masses such as the Río de La Plata, Paranapanema (PB), Luiz Alves, and Kalahari, which developed orogenic belts along the Brazilian and Uruguayan Atlantic coast (e.g. Araçuaí, Ribeira and Dom Feliciano belts; Cordani *et al.* 2016a).

After the Brasiliano orogeny (600–530 Ma), the western margin of the South American continent has been affected by oceanic subduction till today (e.g. Milani & Filho 2000; Martinod *et al.* 2010), but the subduction has no significant impact on the South American platform (Fig. 1). Since ∼135 Ma (Janasi *et al.* 2011), large volumes of basalt lava were extruded from the Tristan–Gough plume and formed the Paraná–Etendeda LIP (red shaded, Fig. 1) (Renne *et al.* 1992; Peate 1997; Granot & Dyment 2015; Svensen *et al.* 2018), and then West Gondwana broke up and South America separated from Africa in Cretaceous.

3. DATA

3.1. Data source and RF processing

We measured the crustal anisotropy of the South American platform using *Pms* data from receiver functions (RFs) by collecting seismic waveforms recorded by 66 broad-band seismic stations of the Brazilian National Seismological Network (RSBR) in the platform region (Bianchi *et al.* 2018) between 2015 and 2019 (red triangles in Fig. 1), and by three portable seismic stations newly installed by the University of São Paulo, University of Brasília and University of the Republic (Uruguay) between 2021 and 2023 (blue triangles in Fig. 1). To ensure high signal-to-noise ratios of the data and to avoid phase triplication, waveforms for earthquakes with magnitudes of > 5.5 and epicentral distances of 30°–95° were selected. The azimuthal distribution of earthquakes around the stations is well balanced (Fig. 2), making it suitable for using the harmonic variation in the *Pms* data from multiple backazimuths (BAZs).

The raw seismic records were firstly processed by the removal of instrument response, averaging, de-trending and coordinate rotation from the ZNE recording system (vertical, N–S horizontal and E–W horizontal) to the ZRT system (vertical, radial and tangential). Secondly, a width factor of Gaussian pulses of 3 ($\alpha = 3$) was applied to perform iterative time-domain deconvolution calculations (Ligorría & Ammon 1999) on the radial and vertical components to produce *R*-component RFs with a central frequency of ∼1.5 Hz, as well as on the tangential and vertical components to produce *T*-component RFs. Then, the *R*-component RFs were visually checked to remove those with unclear *Pms* phases or with strong high-frequency noise. As the *Pms* waves on *T*-component RFs are weak, we did not visually check the *T*-component RFs but took the *T*-component counterpart of all the valid *R*-component RFs as valid. The number of valid RFs for each station varies from 36 to 261, with a mean of 129, which guarantees at least four observations in each quadrant. Finally, to avoid the possibility of misinterpreting time-shifts caused by different epicentral distances as structure, all of the high-quality RFs were moveout corrected to the same reference epicentral distance of 67° (around the middle of the epicentral distance range of 30°–95°, Yuan *et al.* 1997) by using the IASP91 velocity model (Kennett & Engdahl 1991). Figs 3(a) and (b) show the *R*- and *T*-component RFs binned by a BAZ interval of 10° for the ARAG and ITTB stations (Fig. 1), respectively. Observed RFs for more stations are provided in the Supporting Information (Figs S1–S4).

3.2. Harmonic feature of RFs for anisotropic crust

To better understand the appearance feature of the observed RFs shown in Fig. 3, we generate synthetic seismograms by Raysum (Frederiksen & Bostock 2000) and processed the RFs by time-domain deconvolution (Ligorría & Ammon 1999) for a given isotropic and anisotropic crustal model. Figs 4(a) and (b) show the simulated RFs for isotropic and anisotropic crust models, respectively. The *Pms* phase appears only in the *R*-component RFs for isotropic crust, and the *T*-component counterpart is almost zero (red line in Fig. 4a). In contrast, the *Pms* phase from anisotropic crust appears in both the *R*- and *T*-component RFs, as part of the energy in the *R*-component is polarized to the *T*-component owing to splitting (Fig. 4b).

Fig. 5 is the same as Fig. 4, but for observations from different observation directions or BAZs. For isotropic crust, *Pms* arrivals in the *R*-component do not vary with BAZ, and the amplitude of the *T*-component is zero (Fig. 5a). For anisotropic crust with a horizontal axis of symmetry, Moho-converted waves from different observation directions or BAZs at the same station will exhibit harmonic variation in the *R*- and *T*-components with a period of 180° (Maupin & Park 2007; Bianchi *et al.* 2010; Licciardi *et al.* 2018). As shown in Fig. 5(b), *Pms* arrivals in the *R*- and *T*-components vary periodically with BAZ. In cases where the RFs contain noise, the *Pms* phase from a single BAZ may be masked by noise (Fig. 4c). However, the harmonic feature of the *Pms* phase from different BAZs is still observable (Fig. 5c), which can be used to extract crustal anisotropic parameters.

When we look back at the observed RFs in Fig. 3, we find that the *Pms* arrivals on the *R*-component for the ARAG station vary with

Figure 2. Azimuthal distribution of earthquakes (circles) used in this study. The triangle denotes the centre of the seismic stations. For each station, only the earthquakes with epicentral distance between 30° and 95° are used.

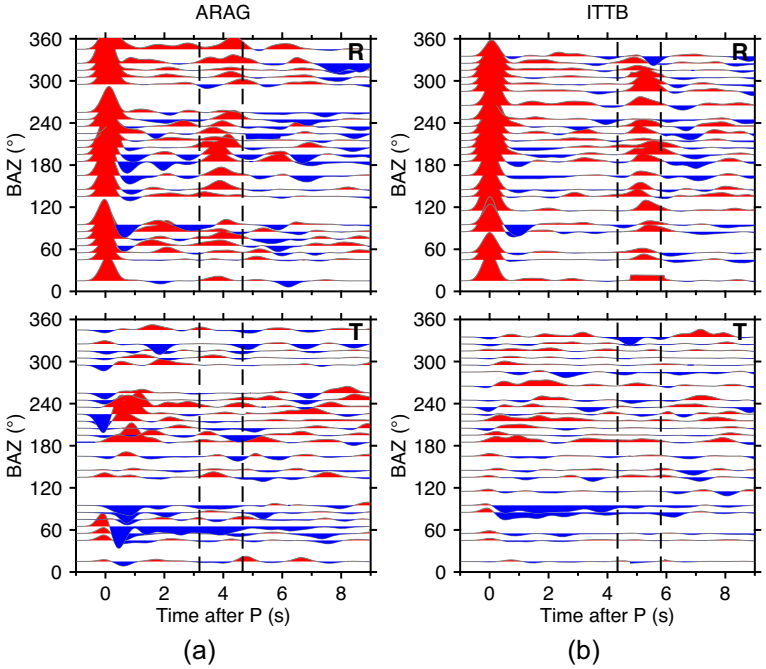

Figure 3. RFs for the (a) ARAG and (b) ITTB stations. Dashes mark the windows representing the predicted *Pms* phase arrivals based on the known crustal thickness from previous studies (Rivadeneyra-Vera *et al.* 2019; Cedraz *et al.* 2020).

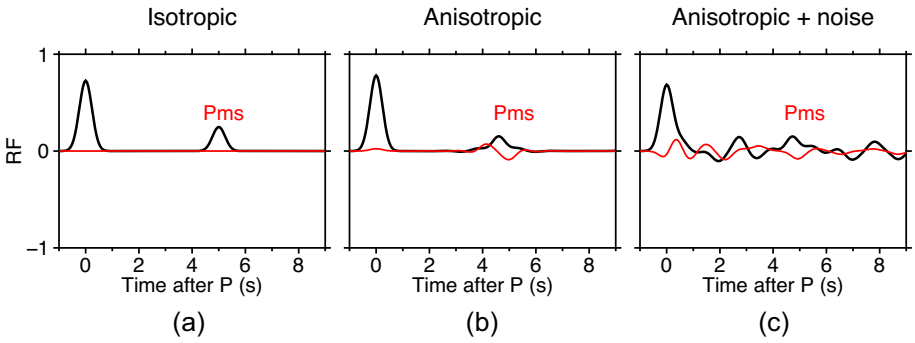

Figure 4. *R*-component (black line) and *T*-component (red line) RFs for (a) isotropic and (b) anisotropic crust. (c) Same as (b), but with random noise.

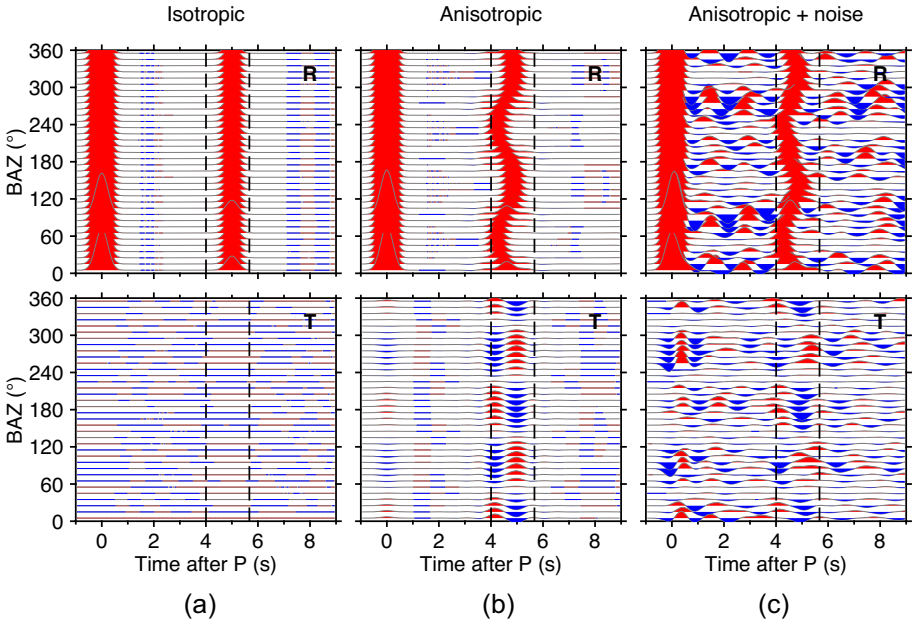

Figure 5. *R*-component (top) and *T*-component (bottom) RFs from multiple BAZs for (a) isotropic and (b) anisotropic crust. (c) Same as (b), but with random noise. Windows marked by dashed lines are the theoretical arrivals of *Pms* phases.

BAZ, and the amplitude of the *T*-component is observable, possibly indicating a strong crustal anisotropy beneath the station. However, the *Pms* arrivals on the *R*-component for the ITTB station do not vary substantially with BAZ, and the amplitude of the *T*-component is small, possibly indicating no or weak crustal anisotropy beneath the station.

4. METHOD

4.1. Extract anisotropic parameters by JOF

Parameters of crustal anisotropy can be extracted from RFs because *P*-to-*S* converted waves are split during propagation through an anisotropic crust. Splitting of the *P*-to-*S* converted waves can be described by the fast polarization direction φ and the delayed time of slow waves τ. As the set of fast and slow waves is polarized from the same incident wave, one would expect the maximum and minimum amplitude in the *R*- and *T*-components before polarization, respectively. Therefore, within a given search range of φ and τ at a certain searching step, the best solution of (φ, τ) can be estimated by maximizing the amplitude of the anisotropy-corrected *R*-component waves or minimizing the amplitude of the anisotropy-corrected *T*-component waves. The rotation-correlation (Vinnik *et al.* 1984), minimum-energy and minimum-eigenvalue methods and their modified versions (e.g. Silver & Chan 1991; Zang *et al.* 2023) are suitable for retrieving anisotropy from single-BAZ observations. However, the Moho-converted *Pms* phase is easily affected by noise (Fig. 4c) and by a dipping Moho (Bianchi *et al.* 2010). Therefore, the extraction of crustal anisotropy parameters by methods that using single-BAZ observations may not be a good choice.

The amplitude and arrival time of the *Pms* phase at a single station exhibit harmonic variation with a period of 180° with respect to BAZ (Fig. 5b), which is another typical characteristic of RFs for anisotropic crust. Using this harmonic feature in multiple-BAZ observations can make the anisotropic parameter solutions more stable compared with the splitting characteristics of single-BAZ observations. For a dipping Moho, the *Pms* phase also exhibits harmonic variation with respect to BAZ, but with a 360° period. In cases where the signal-to-noise ratio is high, the harmonic variation in the *Pms* phase can be used to distinguish between crustal anisotropy and a dipping Moho. In cases where the signal-to-noise ratio is low and where crustal anisotropy and a dipping Moho exist simultaneously, a trade-off between crustal anisotropy and a dipping Moho

may bias the anisotropic solution even if the harmonic variation is considered. So, many studies tried to remove or fit the harmonic effect to obtain more stable isotropic structures (e.g. Shen *et al.* 2013; Deng *et al.* 2015; Li *et al.* 2019; Feng 2021; Feng & Diaz 2023), rather than resolving the anisotropic and/or dipping interface structures.

Liu & Niu (2012) proposed a joint objective function (JOF) analysis method for crustal anisotropy by using multiple-BAZ *R*- and *T*-components of the *Pms* phase under the assumption of a horizontal Moho. This method works well in cases where the fluctuation in the depth of the Moho is small. Wang *et al.* (2020) adapted the JOF method so that crustal anisotropy (φ and τ) and Moho geometry (strike and dip angle) can be simultaneously determined from multiple-BAZ *Pms* phases. However, the adapted JOF method requires a 4-D (four-parameter) grid search, and the computational cost is much higher than that in the case of the JOF method. Both the JOF and the adapted JOF analysis methods require the use of the harmonic variation in multiple-BAZ *Pms* phases to constrain anisotropic parameters, which means that the BAZ distribution of *Pms* observations can influence the solution's reliability. Given that there is no marked fluctuation in Moho depth in the South American platform (Assumpção *et al.* 2013; Rivadeneyra-Vera *et al.* 2019), we favour the more efficient JOF method over the adapted JOF method in this study. A brief review of the principles of the JOF method is presented below. A detailed mathematic derivation has been presented by Liu & Niu (2012).

The JOF method searches within a given range of fast polarization direction (φ) and splitting time (τ) with a defined step, and the set of parameters that best fits the objective function is the solution. The objective function of the JOF method is obtained by the weighted sum of three independent objective functions: (1) removing anisotropic effect from the *R*-component *Pms* by the given set of anisotropic parameters to maximize the stack of the corrected *R*-component *Pms* (denoted as 'Max. Rsum'); (2) removing anisotropic effect from all *R*- and *T*-component *Pms* to maximize the cross-correlation of the corrected *R*-component *Pms* (denoted as 'Max. Rcc') and (3) removing anisotropic effect from all *R*- and *T*-component *Pms* to minimize the stack of the corrected *T*-component *Pms* (denoted as 'Min. Tsum'). The JOF considers both the correlation and periodicity of *R*- and *T*-component *Pms*, which can greatly improve the signal-to-noise ratio. In this study, the search range and step for φ were 0°–180° and 5°, respectively. Considering that the splitting time of the *Pms* phase varies from ∼0.2 s in stable basin regions (e.g. Chen *et al.* 2013) to ∼0.7 s in seismically active regions (e.g. Nagaya *et al.* 2008), with a global average of less than ∼0.3 s (Savage 1999), the search range and step for τ were set as 0–1 and 0.025 s, respectively. A bootstrap statistical method was used to evaluate the solution. One hundred inversions were conducted for each station by randomly selecting 70 per cent of the *Pms* observations. The statistical standard deviation was adopted as the uncertainty of the solution. Considering that the signal-to-noise ratio of the *R*-component *Pms* is normally higher than that of the *T*-component, the weights of the three independent objective functions were set as 0.4, 0.4 and 0.2, respectively. Tests (not shown here) have shown that different weights can weakly change the absolute value of the uncertainty but have little impact on the relative magnitude of the uncertainty among different stations nor on the anisotropic parameter (Liu & Niu 2012). The width of the time window for marking *Pms* phases has a slight influence on JOF results. Considering that the width of the *Pms* phase is inversely proportional to the Gaussian width factor α, we set the time window as $[-2.4/\alpha, 2/\alpha]$ relative to the *a priori* predicted *Pms* arrival, by trial and error. Examples in Figs 3 and 5 show that the adopted time window identified the *Pms* phases in the *R*- and *T*-components reasonably well.

4.2. Synthetic testing

For the JOF method, the signal-to-noise ratio, presence of dipping interfaces, and completeness of the data with respect to BAZs are key influences on the reliability of the solution. To assess how these three aspects influenced the results of the JOF method in the present study, we used the Raysum program (Frederiksen & Bostock 2000) to generate three-component synthetic seismic waves from a complete distribution of observed BAZs (0°–360°) with an interval of 10° for a defined anisotropic crustal model (crustal thickness of 40 km, fast polarization direction of 45°, intensity of shear wave velocity anisotropy of 5 per cent with a theoretical splitting time of 0.55 s, with the model termed 'A45'). Then, synthetic RFs were calculated using the same Gaussian width parameter ($\alpha = 3$) applied to the observed data in the time-domain deconvolution (Ligorría & Ammon 1999). Finally, the JOF method was applied to the synthetic RFs to extract (output) the crustal anisotropic parameters of the input model. The performance of the JOF method under different situations was evaluated by comparing the output and input anisotropic models.

4.2.1. Noise

Fig. 6 shows the synthetic RFs without and with random noise (Figs 6a and b), as well as the results of JOF analysis (Figs 6c and d). The amplitude of the random noise was set as 1.5 × the maximum amplitude of the *T*-component *Pms*. For the noise-free case (Fig. 6c), the extremes of the three independent objective functions (Max Rsum, Max Rcc and Min Tsum) calculated using the JOF almost coincide with the input parameters. For the noise-contaminated case (Fig. 6d), the extremes of the independent objective functions calculated using the JOF deviate substantially from the theoretical input model. Noise affects the splitting time τ and its uncertainty, but not in the fast polarization direction (φ), meaning that the fast polarization direction from the JOF analysis has better reliability than the splitting time.

4.2.2. Dipping sedimentary layer

The amplitudes of the *T*-components of the ARAG and ITTB stations at zero time (Fig. 3) show a regular positive–negative variation with respect to BAZ, which is a typical feature of a dipping interface below stations (McNamara & Owens 1993; Bianchi *et al.* 2010; Tan *et al.* 2018). However, the depth of the dipping interface is not definite. Fortunately, the crustal thickness of the South American platform shows only minor lateral variations, which means that no marked Moho dip exists in the platform (Feng *et al.* 2007; Lloyd *et al.* 2010; Assumpção *et al.* 2013; Rivadeneyra-Vera *et al.* 2019). Considering that the two stations are located at the edges of sedimentary basins (Fig. 1), the dipping interface inferred from the amplitudes of the *T*-components may correspond to shallow sedimentary layers rather than the Moho.

To verify whether crust anisotropy can be affected by overlain dipping sedimentary layer, we generated another synthetic model similar to A45 in Fig. 6, but added a 1-km-thick dipping sedimentary layer with a strike of 180° and dip angle of 15° on its upper surface (with the model termed 'SD180A'). The same synthetic

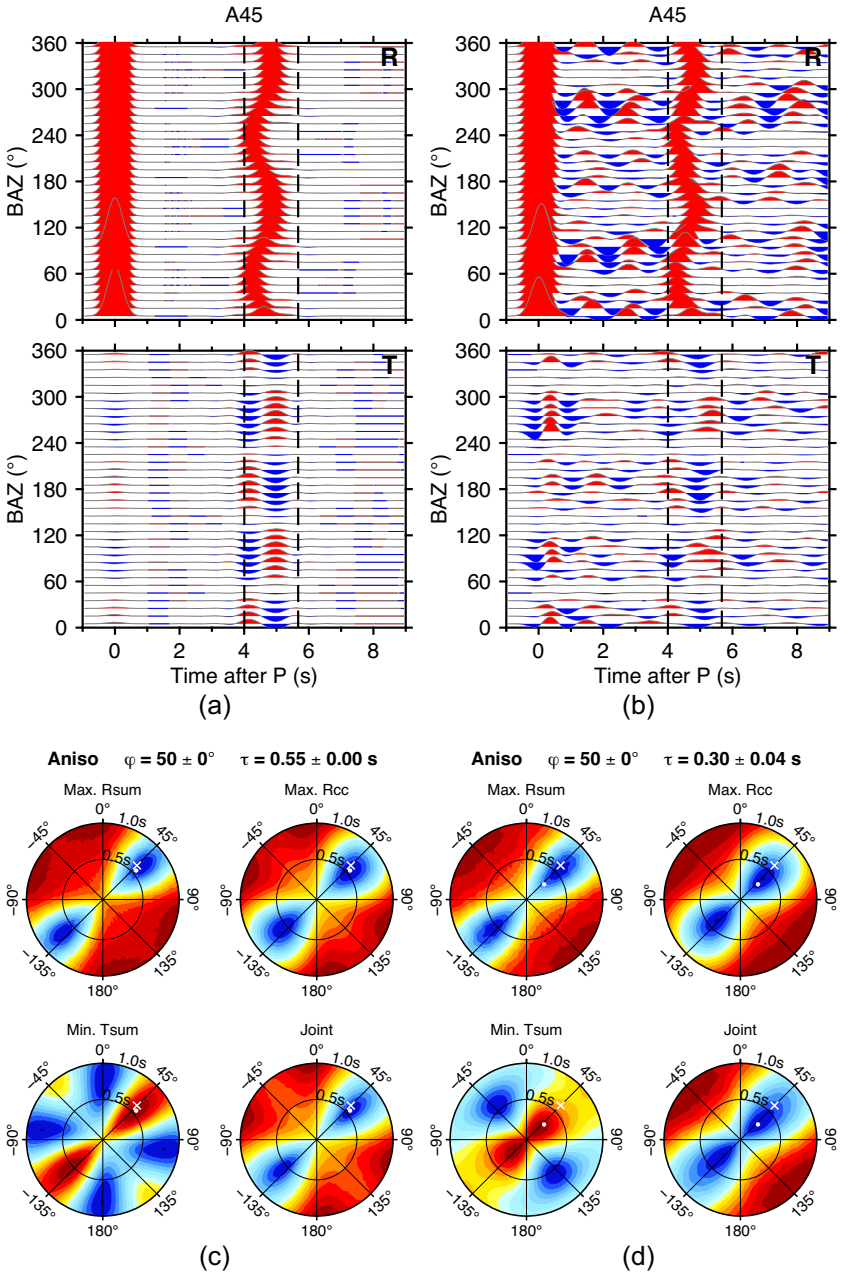

Figure 6. Synthetic RFs for a crustal anisotropic model (a) without and (b) with noise, and their corresponding JOF analysis results (c) and (d), which show the results of anisotropic analysis by using the three independent objective functions (Max Rsum, Max Rcc and Min Tsum) and the JOF method (Joint). The colour gradient from blue to red is scaled to values between 1 and −1, representing the normalized objective function values. White crosses and dots denote the input and final output (inverted) anisotropic parameters, respectively. The final solution and uncertainty of the JOF analysis are labelled at the top of panels (c) and (d).

test as that presented in Fig. 6 was then applied to model SD180A, the results of which are shown in Fig. 7. The *T*-component RFs for arrival times of 0–2 s in Figs 7(a) and (b) exhibit a periodic positive–negative variation with BAZ, similar to the observed data in Fig. 3. However, the *Pms* phase in the range of 4–6 s does not appear to be substantially affected by the dipping sedimentary layer. For the noise-free case (Fig. 7c), the extremes of the independent objective functions calculated using the JOF method almost coincide with the theoretical input model parameters, consistent with the results for the model without a dipping sedimentary layer (A45) (Fig. 6c). For the noise-contaminated case (Fig. 7d), the extremes of the independent objective functions and JOF deviate substantially from the theoretical input model parameters. A comparison of Figs 6(d) and 7(d) reveals that the dipping sedimentary layer increases the misfit between the inverted fast polarization direction (030°) and the theoretical input model (045°), but the misfit of 15° is still within a reasonable range (smaller than a half-quadrant). Regardless of the existence of a dipping sedimentary layer, the fast polarization direction determined by the JOF method is more reliable than the splitting time. Further tests that involved changing the anisotropy intensity (i.e. splitting time) in the theoretical model showed that the JOF method cannot restore the absolute splitting time but can restore the variation trend of intensity. Therefore, when analysing the results of anisotropic intensity given by the JOF method, it is

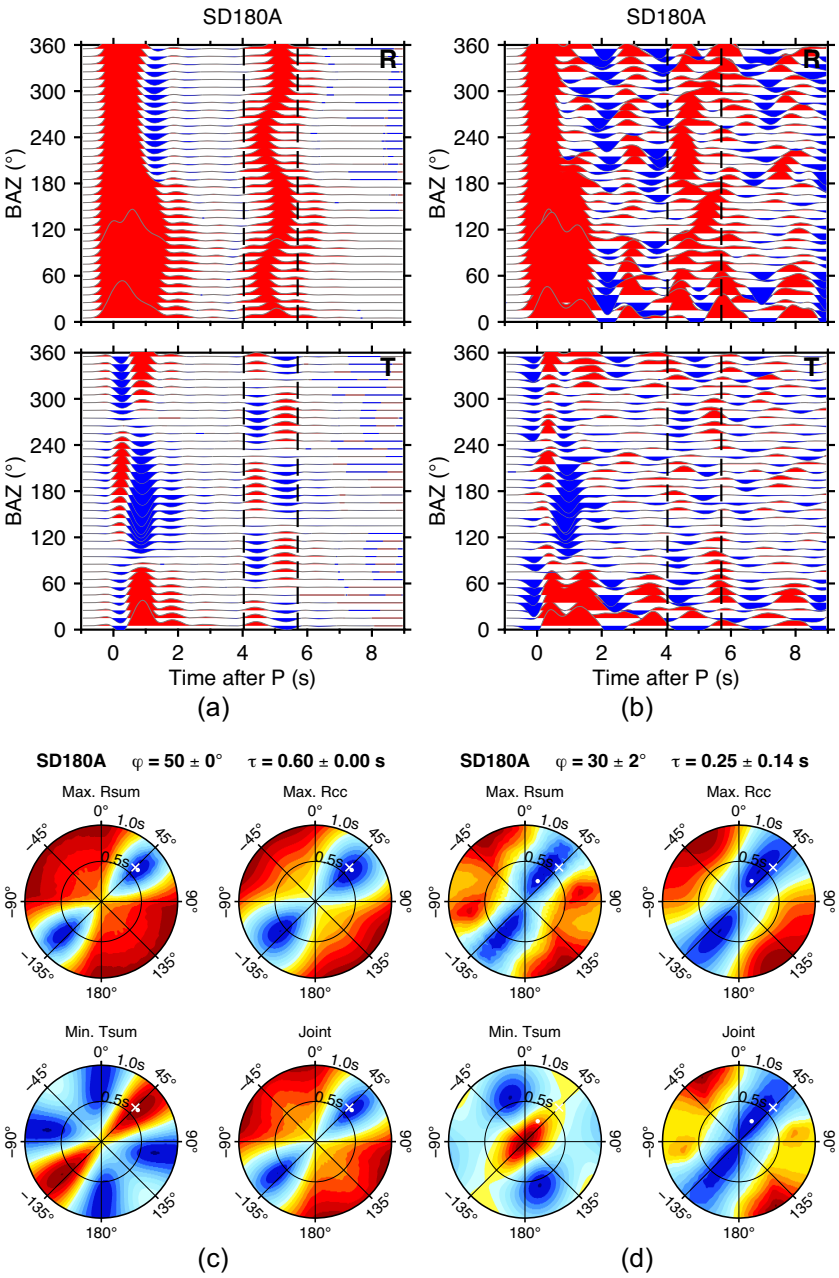

Figure 7. Same as Fig. 6, but for a crustal anisotropic model with an overlying dipping sedimentary layer.

recommended that the comparative anisotropic intensity among different seismic stations should be considered, but not the absolute intensity at a single station.

4.2.3. Completeness of BAZ coverage

As the JOF method fits the harmonic variation in RFs with respect to BAZ, the better the coverage of observed BAZ, the more reliable the solution. The BAZ coverage for the synthetic RFs in the tests presented in Figs 6 and 7 is highly uniform and complete (i.e. observations are available for all directions from 0° to 360°). However, in real studies the BAZ coverage of observations depends on the earthquakes' distribution around seismic stations. There are fewer earthquakes to the south and southeast of the South American platform than to the west and northwest (Fig. 2). We, therefore, performed a similar synthetic test to that presented in Fig. 7, but using part of the synthetic RFs from real BAZs for seismic stations in the South American platform, with results of this analysis being presented in Fig. 8. A comparison of Figs 7(d) and 8(d) reveals that the lack of observed BAZs results in a change in the fast polarization direction from 030° to 035°, which is negligible (equivalent to one searching step), and that the splitting time and its uncertainty change substantially from 0.25 to 0.45 s and from 0.14 to 0.18 s, respectively.

In summary, the results of the synthetic tests presented in Figs 6–8 show that the JOF method can effectively extract crustal anisotropic parameters for a simple crustal model and for a complex crustal model (i.e. one with a dipping sedimentary layer) by using either complete or incomplete BAZ observations. Our testing also shows that the fast polarization direction is less affected by noise, by

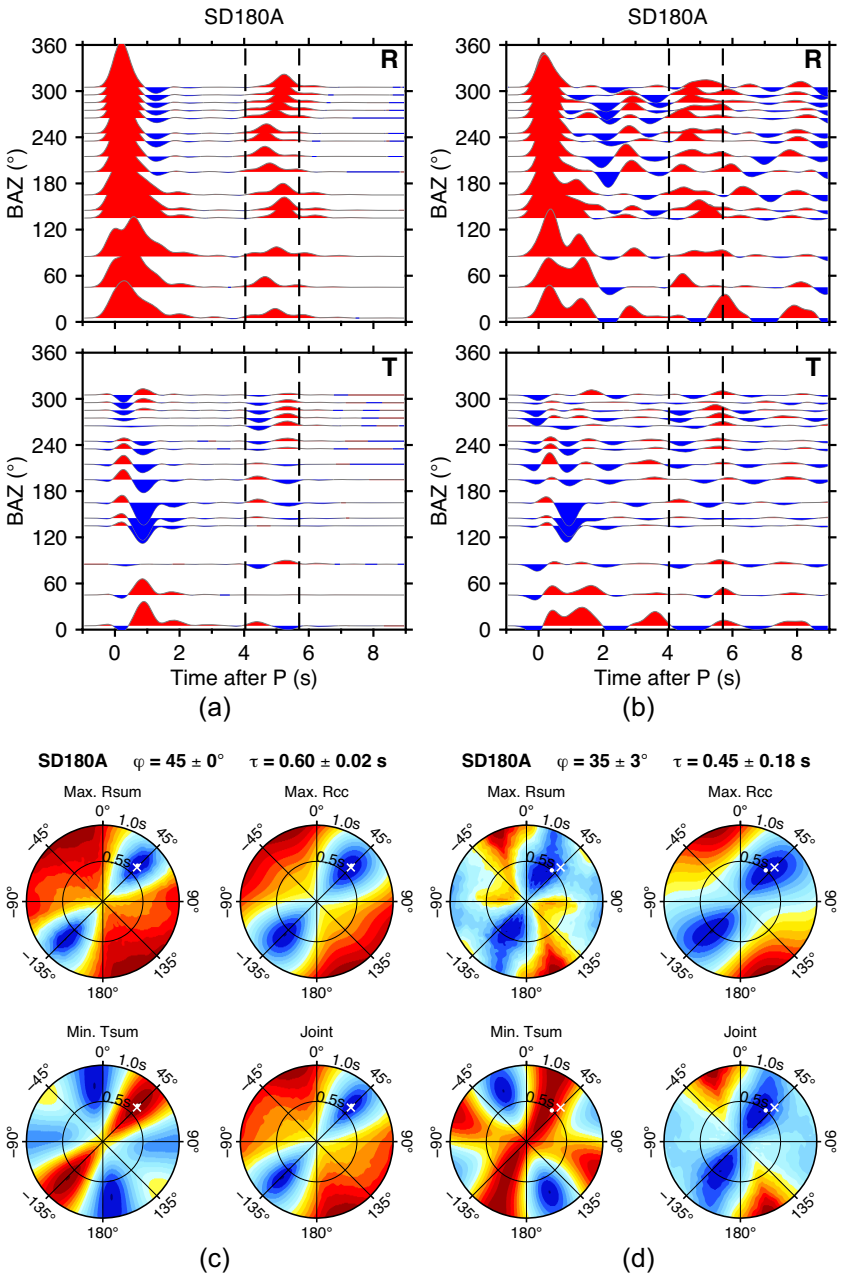

Figure 8. Same as Fig. 7, but with the distribution of observed BAZs for the South American platform.

dipping sedimentary layers, and by the degree of completeness of observed BAZs compared with the splitting time. Therefore, the discussion of results of JOF analysis should focus more on the fast polarization direction and on the comparative intensity of the splitting time at different measuring sites/stations rather than on the absolute splitting time.

5. RESULTS

Fig. 9 shows examples of results of JOF analysis for the ARAG and ITTB stations. The anisotropy of the crust beneath the ARAG station ($\tau = 0.36$ s) is much stronger than that beneath the ITTB station ($\tau = 0.02$ s), consistent with the stronger harmonic variation in the *Pms* phase at the former than the latter (Fig. 3). A half-quadrant (i.e. 22.5°) has previously been used as a measure of fast polarization direction consistency (Wüstefeld & Bokelmann 2007), with solutions with $\delta\varphi \geq 22.5^\circ$ being considered inconsistent. Although the splitting time of crustal anisotropy in different regions of the world does not exceed 0.3 s on average (Savage 1999), the synthetic tests presented in Figs 7 and 8 with $\delta\tau$ of 0.14–0.18 s are able to reliably extract the fast polarization directions. Therefore, we regard solutions with $\delta\tau \leq 0.15$ s as consistent. Solutions for crust with no or weak anisotropy are difficult to determine and may have large misfit and uncertainty as shown by the synthetic test in the Supporting Information (Fig. S5). We therefore regard solutions with weak anisotropy ($\tau \leq 0.15$ s) and solutions with $\delta\varphi \leq 22.5^\circ$ and $\delta\tau \leq 0.15$ s as reliable results.

With respect to the above considerations, we obtained 53 effective measurements of crustal anisotropic parameters (φ and τ) and their uncertainties ($\delta\varphi$ and $\delta\tau$) for the South American platform (Fig. 10

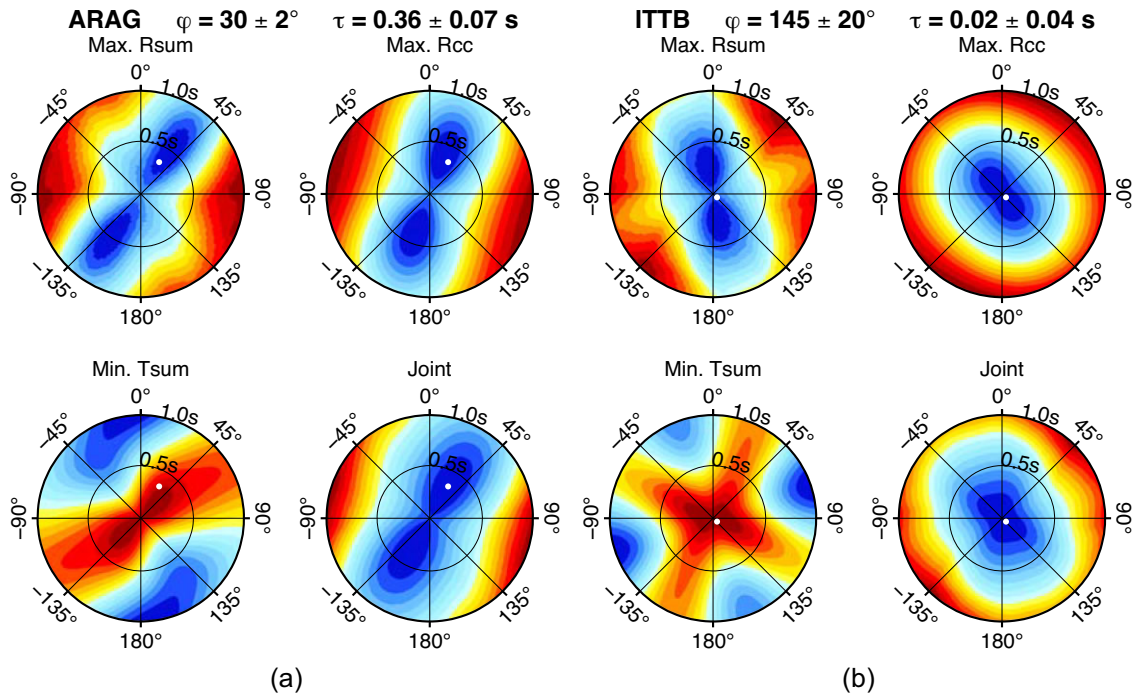

Figure 9. JOF analysis results for the (a) ARAG and (b) ITTB stations. Labels and colour scales are the same as in Fig. 6.

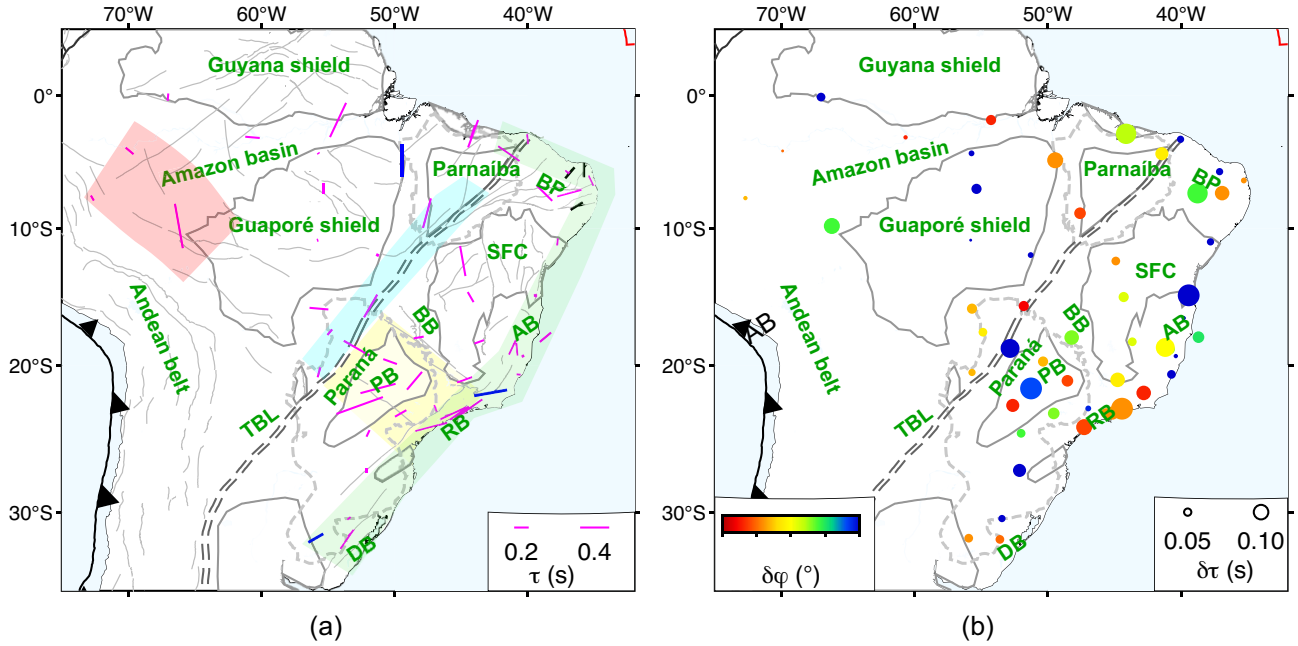

Figure 10. (a) Crustal anisotropy and (b) its uncertainty for the South American platform. In (a), the three blue bars depict results for the three new portable seismic stations using data between 2021 and 2023; the magenta bars represent results for the RSBR stations using data between 2015 and 2019; the three black bars in the BP of NE Brazil are the fast polarization directions of upper-crustal anisotropy from previous local earthquake *S*-wave splitting analyses (do Nascimento *et al.* 2002, 2004; Lopes *et al.* 2010), and their splitting times are smaller than 0.1 s and not to scale; grey lines are faults and magnetic lineaments from the 1:5 000 000 scale Tectonic Map of South America (Cordani *et al.* 2016b). AB = Araçuaí Belt, BB = Brasília Belt, BP = Borborema Province, DB = Dom Feliciano Belt, PB = Paranapanema block, RB = Ribeira Belt, SFC = São Francisco Craton and TBL = Transbrasiliano Lineament.

and Table 1). The three blue bars in Fig. 10(a) depict results for the three portable seismic stations using data between 2021 and 2023, whereas the magenta bars represent results for the RSBR stations using data between 2015 and 2019. The portable stations recorded different earthquakes and have different numbers of observations compared with the RSBR stations, but the three blue bars have fast polarization directions and splitting times that are consistent with their respective adjacent magenta bars (Fig. 10), implying the consistency of the regional anisotropic structures revealed by our results.

Table 1. Results of crustal anisotropy

Station	Lon (°)	Lat (°)	Elev. (m)	φ (°)	$\delta\varphi$ (°)	τ (s)	$\delta\tau$ (s)
AQDB	−55.6997	−20.4758	158	15	7	0.14	0.05
BB19B	−48.5279	−21.0662	571	40	4	0.32	0.08
BSCB	−44.7635	−20.9984	935	70	9	0.22	0.10
BSFB	−40.8465	−18.8313	185	175	13	0.18	0.07
C2SB	−52.8377	−18.7688	757	120	22	0.42	0.13
CLDB	−55.7965	−10.8732	298	75	24	0.02	0.02
CPSB	−53.4432	−30.4123	290	50	20	0.06	0.05
DIAM	−43.6648	−18.2952	1280	70	11	0.14	0.06
ESAR	−44.4403	−23.0207	7	55	6	0.45	0.15
FRTB	−49.564	−23.3439	518	60	13	0.18	0.08
ITAB	−52.1313	−27.2349	459	0	47	0.06	0.09
ITRB	−50.359	−19.7042	426	110	7	0.20	0.07
PARB	−45.6246	−23.3421	777	65	6	0.38	0.07
PCMB	−51.2619	−21.6074	346	75	18	0.50	0.15
PLTB	−53.6044	−31.7637	412	35	5	0.32	0.06
PP1B	−54.8796	−17.6003	368	40	9	0.10	0.06
PTGB	−52.0118	−24.7209	981	25	14	0.10	0.06
SJMB	−41.1847	−18.7029	243	25	10	0.22	0.13
TRCB	−52.6357	−22.7946	490	70	3	0.68	0.09
VABB	−46.9657	−23.0021	866	160	19	0.10	0.04
ARAG	−51.812	−15.706	237	30	2	0.36	0.07
CZSB	−72.7049	−7.7299	196	150	7	0.08	0.03
ETMB	−66.2137	−9.8168	196	170	14	0.62	0.11
IPMB	−48.2117	−17.983	706	80	13	0.14	0.10
ITTB	−55.7343	−4.3672	118	145	20	0.02	0.04
JANB	−44.3112	−15.0581	693	150	11	0.16	0.07
MACA	−60.6838	−3.1615	75	95	3	0.20	0.03
MALB	−54.2649	−1.8529	27	25	3	0.52	0.07
NPGB	−55.3579	−7.0454	266	0	62	0.14	0.07
ROSB	−44.1246	−2.8967	60	20	12	0.40	0.14
SALV	−55.6936	−15.9012	213	95	7	0.26	0.07
SDBA	−44.903	−12.4085	623	170	6	0.42	0.06
SGCB	−67.0306	−0.1223	70	5	52	0.10	0.06
SMTB	−47.5886	−8.8617	292	15	4	0.42	0.08
SNDB	−51.2943	−11.9742	252	25	50	0.04	0.04
TBTG	−69.909	−4.1868	91	130	5	0.14	0.02
NBIT	−39.4346	−14.9307	188	85	44	0.05	0.23
NBLA	−37.789	−10.9925	196	5	54	0.10	0.05
NBLV	−36.9217	−7.3577	602	75	6	0.35	0.10
NBMA	−38.764	−7.3654	436	135	14	0.30	0.14
NBMO	−40.0414	−3.3107	104	175	76	0.14	0.05
NBPA	−37.1121	−5.7503	93	130	26	0.06	0.05
NBPS	−41.4457	−4.394	712	125	9	0.36	0.09
NBPV	−35.2905	−6.4175	89	155	6	0.16	0.04
ABR01	−38.6959	−17.9646	38	50	15	0.20	0.08
ALF01	−40.7252	−20.6169	22	95	22	0.06	0.06
GUA01	−39.8053	−16.5835	198	165	40	0.02	0.03
PET01	−47.2753	−24.2901	150	75	4	0.46	0.11
RIB01	−40.3944	−19.3142	216	150	62	0.04	0.03
SLP01	−45.1559	−23.3243	1117	55	6	0.32	0.09
SIM2	−42.8058	−21.9154	345	80	3	0.46	0.10
VL24	−49.4519	−4.88925	135	0	6	0.44	0.11
TBOT	−55.9373	−31.6827	160	60	6	0.24	0.06

5.1. Uncertainties

The uncertainty of the fast polarization direction ($\delta\varphi$) of the Guyana and Guaporé shields is relatively high (Fig. 10b), which may be related to the weak anisotropy and thus, negligible polarization in these regions. Large $\delta\varphi$ or $\delta\tau$ values are also found in the centre of the Paraná Basin and along the continental margin, possibly associated with sediments in these regions. Relatively small $\delta\varphi$ and $\delta\tau$ values are found along the TBL, in the SFC, along the margin of the Paraná Basin, and in most of the Amazon Basin.

5.2. Crustal anisotropy

The intensity of crustal anisotropy and the fast polarization direction of anisotropy (Fig. 10a) exhibit stronger lateral variations with distinct spatial zoning compared with the azimuthal anisotropy at 40 km depth in South America revealed by global seismic surface wave tomography (Debayle *et al.* 2016, see Fig. S6 in the Supporting Information). These variations are summarized as follows. (i) In the cyan-shaded region in Fig. 10(a), the fast polarization directions are roughly parallel to the strike of the TBL, except for the northeastern

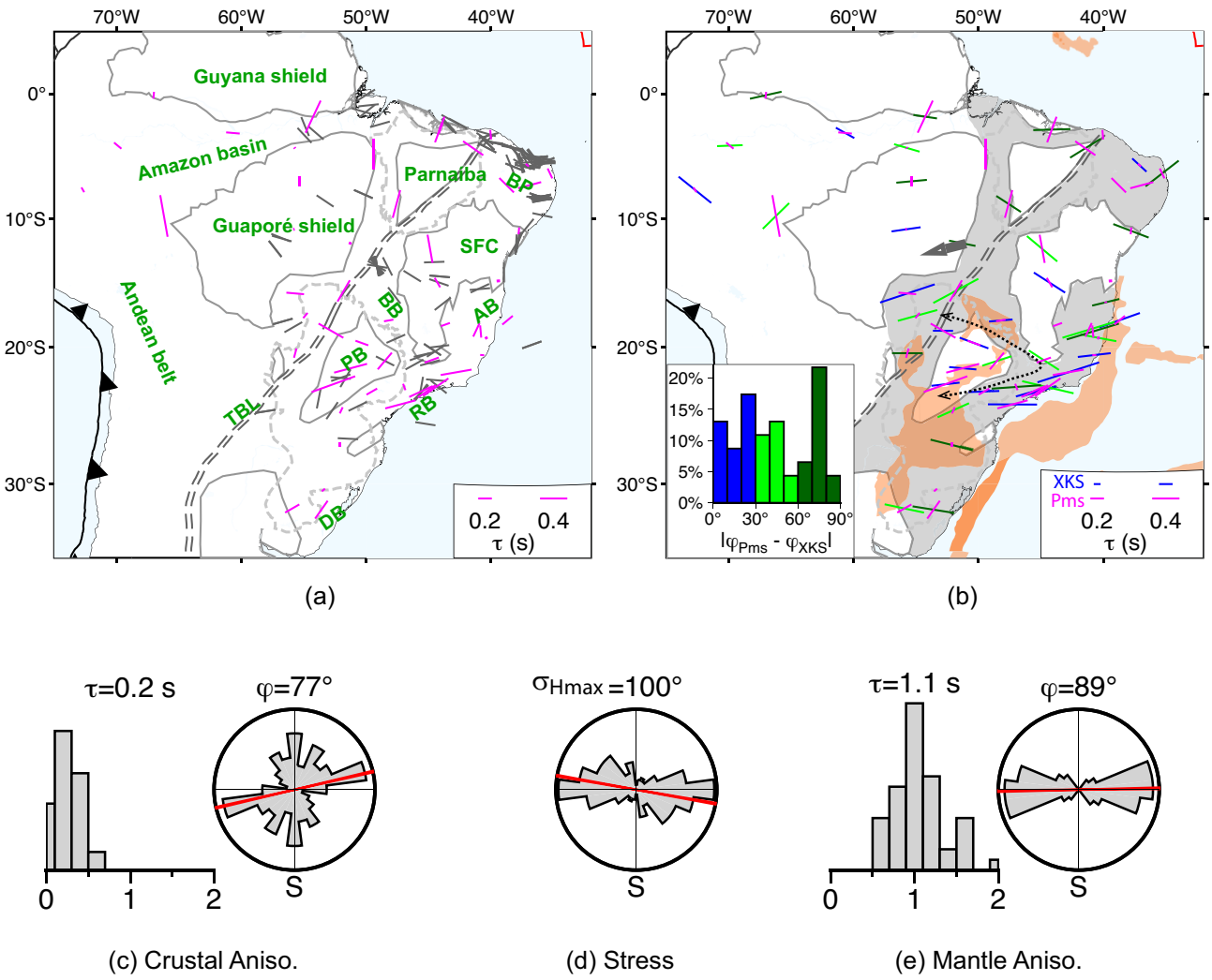

Figure 11. Comparisons of crustal anisotropy (magenta bars) with (a) horizontal principal stress (grey bars) and (b) mantle anisotropy from previous *XKS* splitting analysis (blue, green and dark green bars). Statistics for crustal anisotropy, principal stress and mantle anisotropy for the stable South American platform are given in (c)–(e), respectively, with the overall mean value for each being shown at the top and marked as a red bar in each rose diagram. Data for the horizontal principal stress shown in (a) are from the World Stress Map Database (Heidbach *et al.* 2016). In (b), the thick grey arrow denotes the absolute plate motion direction relative to the hotspot reference model HS3-NUVEL1A (Gripp & Gordon 2002); the black dotted arrow denotes the synchronous rotation trend of the fast directions in the crustal and mantle anisotropy; the shades are the same as Fig. 1; and the inset histogram is the statistics of angle difference between the *XKS* and *Pms* results with blue, green and dark green bars corresponding to small, moderate and large angle differences.

segment close to the continental margin. In contrast, those outside the shaded region are oriented at a high angle to the TBL strike. (ii) The intensity of anisotropy along the passive continental margin in the green-shaded region is very weak, except for the Ribeira Belt in the southeast of this region, and the fast polarization directions tend to be parallel to the continental margin. (iii) In the Paraná Basin and Ribeira Belt (yellow-shaded region in Fig. 10a), the fast polarization directions are mainly WNW–ESE and WSW–ENE, and the intensity of anisotropy is higher than in most of the other regions. (iv) In the western Amazon Basin (red-shaded region), the fast polarization directions are generally consistent with the strike of the Andean orogen. (v) The fast polarization directions in the northern SFC are approximately N–S, whereas those on the southern edge of the SFC are WSW–ENE, similar to those of the Ribeira Belt. (vi) The fast polarization directions vary strongly within BP, similar to the strong heterogeneity of upper-crustal anisotropy previously observed in local earthquake *S*-wave splitting data, as illustrated by the three black bars in Fig. 10(a) (do Nascimento *et al.* 2002, 2004; Lopes *et al.* 2010). (vii) Splitting times for the central Guaporé and southwestern Guyana Shield are too weak to produce dominant polarization directions.

The histogram and rose diagram in Fig. 11(c) give statistics for the splitting time (τ) and fast polarization direction (φ) of crustal anisotropy. The splitting time varies mainly between 0 and 0.5 s, with a regional mean of 0.2 s. The fast polarization directions have a mean of NE (74°, red line in Fig. 11c), with three dominant directions of N–S, SSW–NNE and WSW–ENE.

6. DISCUSSION

Results of the *Pms* splitting analysis reflect the existence of crustal-scale anisotropic structures, and the interpretation of these structures can help to understand dynamic processes within the crust and

across the crust–mantle boundary. To determine the possible mechanisms that have generated the observed crustal anisotropy in the South American platform, which is a tectonically stable region, we analysed the association of crustal anisotropy with tectonic stress (horizontal principal stress, Fig. 11a) and mantle anisotropy from previous *XKS* splitting analysis (Fig. 11b).

6.1. Comparison with geodynamic observations

6.1.1. Tectonic stress

Grey bars in Fig. 11(a) show the distribution of the maximum principal stress field (σ_{Hmax}) in the South America platform based on the World Stress Map Database (Heidbach *et al.* 2016). σ_{Hmax} is oriented mainly E–W, but none of the fast polarization directions of whole-crust anisotropy from our *Pms* analysis (magenta bars in Fig. 10a) or of upper-crustal anisotropy from previous local earthquake *S*-wave analysis (do Nascimento *et al.* 2002, 2004; Lopes *et al.* 2010; black bars in Fig. 10a) shows a strong association with the stress field. The rose diagram in Fig. 11(d) displays the statistics of σ_{Hmax} presented in Fig. 11(a). The stress direction is shown in all azimuths but is dominated by the E–W direction. Although the mean direction in ESE (100°) is distinct from the three major clusters of fast polarization direction of crustal anisotropy shown in Fig. 11(c), we cannot rule out the possibility of influence of the current stress field on local-scale anisotropy due to the sparse distribution of our measurements in such a large geologically diverse region.

6.1.2. Mantle anisotropy

Cool-colour (blue, green and dark green) bars in Fig. 11(b) show the distribution of mantle anisotropy extracted from previous *XKS* splitting analysis (James & Assumpção 1996; Heintz *et al.* 2003; Assumpção *et al.* 2006, 2011; Bastow *et al.* 2015; Chagas de Melo *et al.* 2018). Except for the BP in NE Brazil, the lateral variation in the mantle fast polarization directions in the platform is small and shows a WNW–ESE to WSW–ENE rotation trend consistent with that of the crustal fast polarization directions (magenta bars) in the Paraná Basin and Ribeira Belt (denoted by the black dotted arrow in Fig. 11b). The inset histogram is the statistics of angle differences between the *XKS* and *Pms* results, with blue, green and dark green colours indicating small, moderate and large angle differences, respectively. We can see that in Fig. 11(b) most blue bars with small angle difference concentrate in the Paraná Basin and Ribeira Belt. The histogram and rose diagram in Fig. 11(e) display the statistics of splitting time and fast polarization directions of mantle anisotropy presented in Fig. 11(b). The mean splitting time is 1.1 s, slightly higher than the global average of 1.0 s (Savage 1999). The mean fast polarization direction is E–W (89°), which differs by 12° from the average crust anisotropy (77°).

6.2. Tectonic implications

6.2.1. Dynamic metamorphism

The Transbrasiliano–Kandi tectonic corridor consists of the TBL in South America and the KSZ in Africa (Fig. 12a). The corridor was formed during the last tectonic episode of the Brasiliano-Pan African Orogeny (Santos *et al.* 2008; Cordani *et al.* 2013a, b) in association with the formation of the West Gondwana. Substantial strike-slip movement and reactivation along the NNE–SSW-striking TBL have been inferred (Santos *et al.* 2008; Amaral *et al.* 2017).

Fast polarization directions around the TBL (cyan-shaded belt in Fig. 10a) differ from those of neighbouring regions but are primarily parallel to the strike of this shear zone, which suggests that the alignment of crustal minerals and/or tectonic fragments beneath the shear zone differs from that of neighbouring regions. Some splitting times are larger than the global upper-crustal average of 0.2 s (Liu & Niu 2012), implying that the anisotropy detected by the *Pms* data originates from the entire crust. The crustal-scale anisotropy detected by the *Pms* data is parallel or oblique to the trend of TBL inconsistent with the present-day tectonic stress field (Fig. 11a) and with the mantle anisotropy detected by *XKS* (dark green bars along TBL in Fig. 11b). Therefore, the anisotropy along the TBL shear zone is more likely to be related to crustal deformation during the formation of the shear zone and reactivation. Crustal minerals and tectonic fragments beneath the TBL might have become realigned during shear-zone formation and reactivation involving strong dynamic metamorphism and the fragmentation and recrystallization of crustal rocks in the region. Furthermore, the interpretation of seismic tomographic models has suggested that the TBL is a deep shear zone extending down to the lithosphere (e.g. Feng *et al.* 2007; Ciardelli *et al.* 2022), implying that such dynamic metamorphism was sufficiently strong to deform the entire crust, even including part of the lithospheric mantle.

6.2.2. Continental rifting

The passive continental margin along the eastern and northeastern boundaries of the South American platform is seismically inactive at present but represents the location of continental rifting of West Gondwana during the earliest Mesozoic (Cordani *et al.* 2009, Fig. 12). Although the passive continental margin extends for thousands of kilometres, most splitting times of crustal anisotropy (except for the Ribeira Belt) are consistently very small, measuring less than ∼0.1 s (a green-shaded region with a width of ∼250 km in Fig. 10a). The fast polarization directions in the green-shaded region in Fig. 10(a) tend to be oriented along the margin (i.e. parallel to the rift). Except for the Ribeira Belt of southeastern Brazil, the fast polarization directions of crustal anisotropy differ from those of mantle anisotropy along the passive margin (dark green bars in Fig. 11b), implying different deformation regimes for the crust and mantle.

Continental rifts normally have a long history of tectonic extension (Walker *et al.* 2004; Illsley-Kemp *et al.* 2017; Brune *et al.* 2023), which is considered to be one of the main geodynamic mechanisms of structural deformation (Fig. 12b). Studies of deformation processes in the presently active intracontinental rift of the Eastern African Rift System have reported rift-parallel fast polarization directions in both the crust (Illsley-Kemp *et al.* 2017) and the mantle (e.g. Reed *et al.* 2017; Tepp *et al.* 2018; Ebinger *et al.* 2024). As the passive continental margin of the South American platform has not undergone deformation after the breakup of West Gondwana (Cordani *et al.* 2009), it is possible that the rift-parallel fast polarization directions of weak crustal anisotropy were generated by the mild development of extensional strain fabrics during the continental rifting (Fig. 12b), especially in the green-shaded region in BP where tectonic faults are nearly perpendicular to the margin (Fig. 10a).

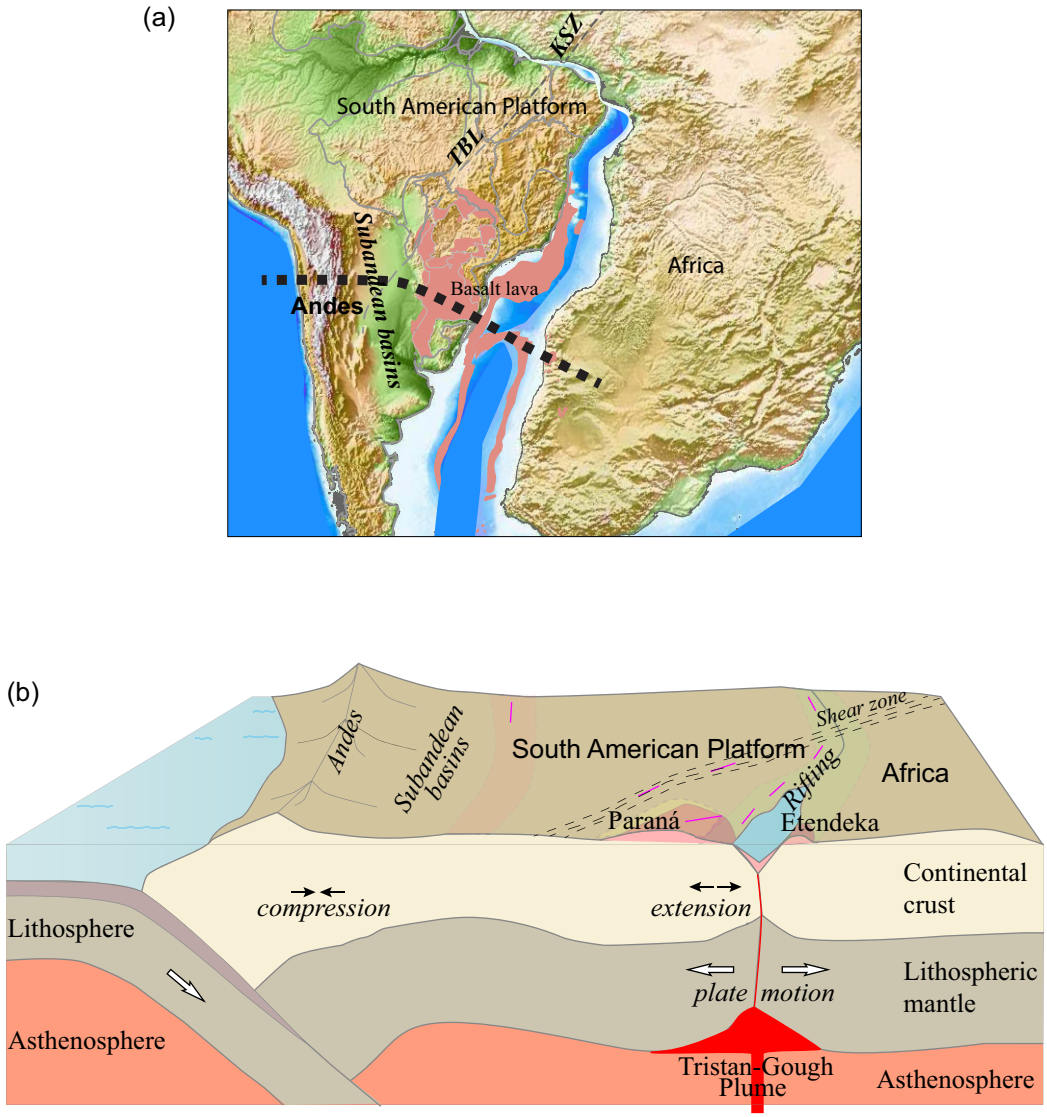

Figure 12. (a) Schematic map of the separation of South American and Africa and (b) corresponding dynamic model. In (a), the present topography is shown; data for the red-shaded basaltic lava are from Coffin *et al.* (2013); thick dashes mark the approximate location of the transect crossing the Paraná–Etendeka LIP shown in (b). TBL = Transbrasiliano Lineament in South America and KSZ = Kandi Shear Zone in Africa. In (b), magenta bars indicate the fast polarization directions of crustal anisotropy; the blue-shaded region labelled 'rifting' corresponds to the region of strong anisotropy observed in this study.

6.2.3. Mantle upwelling

During the initiation of the separation of South America from Africa, large volumes of basalt lava were extruded from the Tristan–Gough plume and formed the Paraná–Etendeda LIP (Renne *et al.* 1992; Peate 1997; Granot & Dyment 2015; Svensen *et al.* 2018, Fig. 12). The mantle upwelling may influence the lithosphere beneath the area covered by LIP, for example, the Paraná Basin and Ribeira Belt.

The fast polarization directions for the crust (magenta bars in Fig. 11b) and for the mantle (cool-colour bars in Fig. 11b) show a similar change in orientation from WNW–ESE to WSW–ENE in the Paraná Basin and the same WSW–ENE orientation in the Ribeira Belt (dotted arrow in Fig. 11b). Similar polarization in crust and mantle can occur under simultaneous or coupled crustal–mantle deformation during the same tectonic event.

Previous studies have demonstrated that fast polarization directions of mantle anisotropy tend to be parallel to and rotate near craton's boundaries, implying that the geometry of the cratons themselves can influence subsequent lithospheric deformation (e.g. Assumpção *et al.* 2011; Tepp *et al.* 2018). So, the rotation trend of fast directions of mantle anisotropy beneath the cratonic Paraná Basin and beneath the Ribeira Belt on the southern border of SFC (dotted arrow in Fig. 11b) may be a result of the combined effect of fossil lithospheric deformation and modern mantle flow. However, the mean splitting times observed for the crust of the Paraná Basin and Ribeira Belt (~0.4 s) are obviously higher than that for the whole platform (0.2 s). An additional mechanism must be causing the strong crustal anisotropy and similar crustal–mantle polarization in the region.

Magmatism during mantle upwelling can result in the formation of high-pressure rocks (e.g. blueschist and/or eclogite) that manifest anisotropy in the middle to lower crust (Cossette *et al.* 2016). Local stress can be changed by underlying magmatic processes and thus disrupt the fast orientation of anisotropy (Bacon *et al.* 2022). So, the similar crustal and mantle fast polarization directions and strong

crustal anisotropy observed in the Paraná Basin and the Ribeira Belt might therefore be related to changes in rock texture or in stress-induced structures caused by magmatism during the breakup of West Gondwana or by the combined effect of fossil lithospheric fabric and modern mantle flow (Fig. 12).

7. CONCLUSION

Parameters of crustal anisotropy for 53 seismic stations in the South American platform were extracted by splitting analysis of teleseismic *P*-wave RFs. Our results show distinct spatial zoning with respect to anisotropic characteristics: (1) fast polarization directions of anisotropy observed near the TBL shear zone tend to be along the strike of the shear zone; (2) anisotropy observed along the passive continental margin in the east and northeast of the platform is weak, but the fast polarization directions tend to be oriented parallel to the margin and (3) fast polarization directions observed in the crust and mantle of the Paraná Basin and Ribeira Belt show a similar WNW–ESE to WSW–ENE rotation trend. The identified crustal anisotropy is not associated with the current tectonic stress field or plate motion direction but is related to the evolution of West Gondwana, including the formation of the large-scale TBL shear zone, tectonic extension during the rifting of West Gondwana, and magmatism during the breakup of West Gondwana.

ACKNOWLEDGMENTS

This work was supported by the Natural Science Foundation of China (grants 41974051 and 42174068), the Basic Research Foundation of the Chinese Academy of Geological Sciences (JKY202217), the Deep Geological Survey Project of the China Geological Survey (DD20230008, DD20221643 and DD20190010) and the São Paulo Research Foundation (FAPESP) thematic project 2013/24215–6.

SUPPORTING INFORMATION

Supplementary data are available at *GJIRAS* online.

Please note: Oxford University Press is not responsible for the content or functionality of any supporting materials supplied by the authors. Any queries (other than missing material) should be directed to the corresponding author for the paper.

DATA AVAILABILITY

Seismic data from the RSBR are available at http://rsbr.on.br/, new observations from the three portable stations are restricted but available on reasonable request. All figures were constructed using Generic Mapping Tools (Wessel *et al.* 2013), available at https://www.generic-mapping-tools.org/. RFs from raw seismic waveforms were retrieved via codes in Computer Programs in Seismology (Herrmann 2013). Synthetic seismograms are made with the Raysum program (Frederiksen & Bostock 2000).

REFERENCES

Amaral, W.S., Kraus, R.K., Dantas, E.L., Fuck, R.A. & Pitombeira, J.P.A. 2017. Sinistral reactivation of the Transbrasiliano Lineament: Structural and geochronological evidences in the Cariré Granulite Zone, Borborema Province—NE Brazil, *J. South Am. Earth Sci.,* **79,** 409–420. https://doi.org/10.1016/j.jsames.2017.08.022

Assumpção, M., Feng, M., Tassara, A. & Julià, J. 2013. Models of crustal thickness for South America from seismic refraction, receiver functions and surface wave tomography, *Tectonophysics,* **609,** 82–96. https://doi.org/10.1016/j.tecto.2012.11.014

Assumpção, M., Guarido, M., van der Lee, S. & Dourado, J.C. 2011. Upper-mantle seismic anisotropy from SKS splitting in the South American stable platform: a test of asthenospheric flow models beneath the lithosphere, *Lithosphere,* **3**(2), 173–180. https://doi.org/10.1130/l99.1

Assumpção, M., Heintz, M., Vauchez, A. & Silva, M.E. 2006. Upper mantle anisotropy in SE and Central Brazil from SKS splitting: evidence of asthenospheric flow around a cratonic keel, *Earth planet. Sci. Lett.,* **250**(1), 224–240. https://doi.org/10.1016/j.epsl.2006.07.038

Bacon, C.A., Johnson, J.H., White, R.S. & Rawlinson, N. 2022. On the origin of seismic anisotropy in the shallow crust of the Northern Volcanic Zone, Iceland, *J. geophys. Res.,* **127**(1), e2021JB022655. https://doi.org/10.1029/2021JB022655

Bastow, I.D., Julià, J., do Nascimento, A.F., Fuck, R.A., Buckthorp, T.L. & McClellan, J.J. 2015. Upper mantle anisotropy of the Borborema Province, NE Brazil: Implications for intra-plate deformation and sub-cratonic asthenospheric flow, *Tectonophysics,* **657,** 81–93. https://doi.org/10.1016/j.tecto.2015.06.024

Becker, T.W., Lebedev, S. & Long, M.D. 2012. On the relationship between azimuthal anisotropy from shear wave splitting and surface wave tomography, *J. geophys. Res.,* **117**(B1), B01306. https://doi.org/10.1029/2011JB008705

Bianchi, I., Park, J., Piana Agostinetti, N. & Levin, V. 2010. Mapping seismic anisotropy using harmonic decomposition of receiver functions: an application to Northern Apennines, Italy, *J. geophys. Res.,* **115**(B12), B12317, https://doi.org/10.1029/2009JB007061

Bianchi, M.B. *et al.* 2018. The Brazilian Seismographic Network (RSBR): improving seismic monitoring in Brazil, *Seismol. Res. Lett.,* **89**(2A), 452–457. https://doi.org/10.1785/0220170227

Brune, S., Kolawole, F., Olive, J.-A., Stamps, D.S., Buck, W.R., Buiter, S.J.H., Furman, T. & Shillington, D.J. 2023. Geodynamics of continental rift initiation and evolution, *Nat. Rev. Earth Environ.,* **4**(4), 235–253. https://doi.org/10.1038/s43017-023-00391-3

Cedraz, V., Julià, J. & Assumpção, M. 2020. Joint inversion of receiver functions and surface-wave dispersion in the Pantanal Wetlands: implications for Basin formation, *J. geophys. Res.,* **125**(2), e2019JB018337. https://doi.org/10.1029/2019JB018337

Chagas de Melo, B., Assumpção, M. & Team, -.B.P. 2018. Mantle anisotropy and asthenospheric flow around cratons in southeastern South America, *Geophys. J. Int.,* **215**(1), 494–506. https://doi.org/10.1093/gji/ggy288

Chen, Y., Zhang, Z., Sun, C. & Badal, J. 2013. Crustal anisotropy from Moho converted Ps wave splitting analysis and geodynamic implications beneath the eastern margin of Tibet and surrounding regions, *Gondwana Res.,* **24**(3), 946–957. https://doi.org/10.1016/j.gr.2012.04.003

Ciardelli, C., Assumpção, M., Bozdağ, E. & van der Lee, S. 2022. Adjoint waveform tomography of South America, *J. geophys. Res.,* **127**(2), e2021JB022575. https://doi.org/10.1029/2021JB022575

Coffin, M.F., Gahagan, L.M., Lawver, L.A. & Dalziel, I.W.D. 2013. *Large Igneous Provinces: Map and Data,* Institute for Geophysics, University of Texas.

Cordani, U.G., Pimentel, M.M., De Araújo, C.E.G., Basei, M.A.S., Fuck, R.A. & Girardi, V.A.V. 2013a. Was there an Ediacaran Clymene Ocean in central South America?, *Am. J. Sci.,* **313**(6), 517–539. https://doi.org/10.2475/06.2013.01

Cordani, U.G., Pimentel, M.M., de Araújo, C.E.G. & Fuck, R.A. 2013b. The significance of the Transbrasiliano-Kandi tectonic corridor for the amalgamation of West Gondwana, *Braz. J. Geol.,* **43**(3), 583–597. https://doi.org/10.5327/Z2317-48892013000300012

Cordani, U.G., Ramos, V.A., Fraga, L.M., Cegarra, M., Delgado, I., de Souza, K.G., Gomes, F.E.M. & Schobbenhaus, C. 2016a. *Explanatory Notes: Tectonic Map of South America,* Second edn, Commission for the Geological Map of the World, Paris.

Cordani, U.G., Ramos, V.A., Fraga, L.M., Cegarra, M., Delgado, I., de Souza, K.G., Gomes, F.E.M. & Schobbenhaus, C. 2016b. *Tectonic Map of South*

America, Second edn, Commission for the Geological Map of the World, Paris.

Cordani, U.G., Sato, K., Teixeira, W., Tassinari, C.C.G. & Basei, M.A.S. 2000. Crustal evolution of the South American platform, in Cordani, U. G., et al., eds, *Tectonic Evolution of South America,* Brazil Federal Mines Department, Rio de Janeiro, pp. 19–40.

Cordani, U.G., Teixeira, W., D'Agrella-Filho, M.S. & Trindade, R.I. 2009. The position of the Amazonian Craton in supercontinents, *Gondwana Res.,* **15**(3), 396–407. https://doi.org/10.1016/j.gr.2008.12.005

Cossette, É., Audet, P., Schneider, D. & Grasemann, B. 2016. Structure and anisotropy of the crust in the Cyclades, Greece, using receiver functions constrained by in situ rock textural data, *J. geophys. Res.,* **121**(4), 2661–2678. https://doi.org/10.1002/2015JB012460

Crampin, S. 1979. Seismic anisotropy in the upper mantle, *Tectonophysics,* **56**(1), 131, https://doi.org/10.1016/0040-1951(79)90026-X

Debayle, E., Dubuffet, F. & Durand, S. 2016. An automatically updated S-wave model of the upper mantle and the depth extent of azimuthal anisotropy, *Geophys. Res. Lett.,* **43**(2), 674–682. https://doi.org/10.1002/2015GL067329

Deng, Y., Shen, W., Xu, T. & Ritzwoller, M.H. 2015. Crustal layering in northeastern Tibet: a case study based on joint inversion of receiver functions and surface wave dispersion, *Geophys. J. Int.,* **203**(1), 692–706. https://doi.org/10.1093/gji/ggv321

do Nascimento, A.F., Bezerra, F.H.R. & Takeya, M.K. 2004. Ductile Precambrian fabric control of seismic anisotropy in the Açu dam area, northeastern Brazil, *J. geophys. Res.,* **109**(B10), B10311, https://doi.org/10.1029/2004JB003120

do Nascimento, A.F., Pearce, R.G. & Takeya, M.K. 2002. Local shear wave observations in João Câmara, northeast Brazil, *J. geophys. Res.,* **107**(B10), ESE 8–1-ESE 8-9. https://doi.org/10.1029/2001JB000560

Ebinger, C.J., Reiss, M.C., Bastow, I. & Karanja, M.M. 2024. Shallow sources of upper mantle seismic anisotropy in East Africa, *Earth planet. Sci. Lett.,* **625,** 118488, https://doi.org/10.1016/j.epsl.2023.118488

Feng, L. 2021. High-resolution crustal and uppermost mantle structure beneath Central Mongolia from rayleigh waves and receiver functions, *J. geophys. Res.,* **126**(4), e2020JB021161, https://doi.org/10.1029/2020JB021161

Feng, L. & Diaz, J. 2023. A high-resolution shear velocity model of the crust and uppermost mantle beneath Westernmost Mediterranean including radial anisotropy, *J. geophys. Res.,* **128**(9), e2023JB026868, https://doi.org/10.1029/2023JB026868

Feng, M., van der Lee, S. & Assumpção, M. 2007. Upper mantle structure of South America from joint inversion of waveforms and fundamental mode group velocities of Rayleigh waves, *J. geophys. Res.,* **112**(B4), B04312, https://doi.org/10.1029/2006JB004449

Frederiksen, A.W. & Bostock, M.G. 2000. Modelling teleseismic waves in dipping anisotropic structures, *Geophys. J. Int.,* **141**(2), 401–412, https://doi.org/10.1046/j.1365-246x.2000.00090.x

Gao, Y., Shi, Y., Wu, J. & Tai, L. 2012. Shear-wave splitting in the crust: regional compressive stress from polarizations of fast shear-waves, *Earthq. Sci.,* **25**(1), 35–45, https://doi.org/10.1007/s11589-012-0829-3

Gao, Y., Wu, J., Yi, G. & Shi, Y. 2010. Crust-mantle coupling in North China: Preliminary analysis from seismic anisotropy, *Chin. Sci. Bull.,* **55**(31), 3599–3605, https://doi.org/10.1007/s11434-010-4135-y

Granot, R. & Dyment, J. 2015. The Cretaceous opening of the South Atlantic Ocean, *Earth planet. Sci. Lett.,* **414,** 156–163, https://doi.org/10.1016/j.epsl.2015.01.015

Gripp, A.E. & Gordon, R.G. 2002. Young tracks of hotspots and current plate velocities, *Geophys. J. Int.,* **150,** 321–361.

Heidbach, O., Rajabi, M., Reiter, K., Ziegler, M. & Team, W. 2016. World Stress Map Database Release 2016. V. 1.1, *GFZ Data Services,* https://doi.org/10.5880/WSM.2016.001. (Accessed: 10 June 2024).

Heintz, M., Vauchez, A., Assumpção, M., Barruol, G. & Egydio-Silva, M. 2003. Shear wave splitting in SE Brazil: an effect of active or fossil upper mantle flow, or both?, *Earth planet. Sci. Lett.,* **211**(1), 79–95, https://doi.org/10.1016/S0012-821X(03)00163-8

Herrmann, R.B. 2013. Computer programs in seismology: an evolving tool for instruction and research, *Seismol. Res. Lett.,* **84**(6), 1081–1088, https://doi.org/10.1785/0220110096

Illsley-Kemp, F. *et al.* 2017. Extension and stress during continental breakup: seismic anisotropy of the crust in Northern Afar, *Earth planet. Sci. Lett.,* **477,** 41–51. https://doi.org/10.1016/j.epsl.2017.08.014

James, D.E. & Assumpção, M. 1996. Tectonic implications of S-wave anisotropy beneath SE Brazil, *Geophys. J. Int.,* **126,** 1–10, https://doi.org/10.1111/j.1365-246X.1996.tb05263.x

Janasi, V.d.A., de Freitas, V.A. & Heaman, L.H. 2011. The onset of flood basalt volcanism, Northern Paraná Basin, Brazil: a precise U–Pb baddeleyite/zircon age for a Chapecó-type dacite, *Earth planet. Sci. Lett.,* **302**(1), 147–153, https://doi.org/10.1016/j.epsl.2010.12.005

Kennett, B.L.N. & Engdahl, E.R. 1991. Traveltimes for global earthquake location and phase identification, *Geophys. J. Int.,* **105,** 429–465. https://doi.org/10.1111/j.1365-246X.1991.tb06724.x

Li, J., Song, X., Wang, P. & Zhu, L. 2019. A Generalized H-κ Method With Harmonic Corrections on Ps and Its Crustal Multiples in Receiver Functions, *J. geophys. Res.,* **124**(4), 3782–3801. https://doi.org/10.1029/2018JB016356

Licciardi, A., Eken, T., Taymaz, T., Piana Agostinetti, N. & Yolsal-Çevikbilen, S. 2018. Seismic anisotropy in central North Anatolian Fault Zone and its implications on crustal deformation, *Phys. Earth planet. Inter.,* **277,** 99–112. https://doi.org/10.1016/j.pepi.2018.01.012

Ligorría, J.P. & Ammon, C.J. 1999. Iterative deconvolution and receiver-function estimation, *Bull. seism. Soc. Am.,* **89,** 1395–1400. https://doi.org/10.1785/BSSA0890051395

Liu, H. & Niu, F. 2012. Estimating crustal seismic anisotropy with a joint analysis of radial and transverse receiver function data, *Geophys. J. Int.,* **188**(1), 144–164. https://doi.org/10.1111/j.1365-246X.2011.05249.x

Lloyd, S., van der Lee, S., França, G.S., Assumpção, M. & Feng, M. 2010. Moho map of South America from receiver functions and surface waves, *J. geophys. Res.,* **115,** B11315. https://doi.org/10.1029/2009JB006829.

Lopes, A.E.V., Assumpção, M., Do Nascimento, A.F., Ferreira, J.M., Menezes, E.A.S. & Barbosa, J.R. 2010. Intraplate earthquake swarm in Belo Jardim, NE Brazil: reactivation of a major Neoproterozoic shear zone (Pernambuco Lineament), *Geophys. J. Int.,* **180**(3), 1303–1312. https://doi.org/10.1111/j.1365-246X.2009.04485.x

Martinod, J., Husson, L., Roperch, P., Guillaume, B. & Espurt, N. 2010. Horizontal subduction zones, convergence velocity and the building of the Andes, *Earth planet. Sci. Lett.,* **299**(3), 299–309. https://doi.org/10.1016/j.epsl.2010.09.010

Maupin, V. & Park, J. 2007. *1.09–Theory and Observations—Wave Propagation in Anisotropic Media. in Treatise on Geophysics,* ed. Schubert, G., pp. 289–321, Elsevier, Amsterdam.

McNamara, D.E. & Owens, T.J. 1993. Azimuthal shear wave velocity anisotropy in the Basin and Range Province using moho Ps converted phases, *J. geophys. Res.,* **98**(B7), 12003–12017. https://doi.org/10.1029/93JB00711

Milani, E.J. & Filho, A.T. 2000. Sedimentary Basins of South America, in Cordani, U.G., et al., eds, *Tectonic Evolution of South America,* Brazil Federal Mines Department, Rio de Janeiro, pp. 389–449

Nagaya, M., Oda, H., Akazawa, H. & Ishise, M. 2008. Receiver functions of seismic waves in layered anisotropic media: application to the estimate of seismic anisotropy, *Bull. seism. Soc. Am.,* **98**(6), 2990–3006. https://doi.org/10.1785/0120080130

Nicolas, A. & Christensen, N.I. 1987. Formation of anisotropy in upper mantle peridotites—a review, in Fuchs,, K. & Froidevaux,, C.eds, *Composition, Structure and Dynamics of the Lithosphere-Asthenosphere System,* the American Geophysical Union, Washington, DC, pp. 111–123.

Peate, D.W. 1997. The Paraná-Etendeka Province, in Mahoney, J.J. & Coffin, M.F., eds, *Large Igneous Provinces: Continental, Oceanic, and Planetary Flood Volcanism,* the American Geophysical Union, Washington, DC, pp. 217–245.

Reed, C.A., Liu, K.H., Yu, Y. & Gao, S.S. 2017. Seismic anisotropy and mantle dynamics beneath the Malawi Rift Zone, East Africa, *Tectonics,* **36**(7), 1338–1351. https://doi.org/10.1002/2017TC004519

Renne, P.R., Ernesto, M., Pacca, I.G., Coe, R.S., Glen, J.M., Prévot, M. & Perrin, M. 1992. The age of Paraná Flood Volcanism, rifting of Gondwanaland, and the Jurassic-Cretaceous boundary, *Science,* **258**(5084), 975–979. https://doi.org/10.1126/science.258.5084.975

Rivadeneyra-Vera, C. *et al.* 2019. An updated crustal thickness map of Central South America based on receiver function measurements in the Region of the Chaco, Pantanal, and Paraná Basins, Southwestern Brazil, *J. geophys. Res.,* **124**(8), 8491–8505. https://doi.org/10.1029/2018JB016811

Santos, T.J.S.D., Fetter, A.H., Neto, J.A.N., Pankhurst, R.J., Trouw, R.A.J., Neves, B.B.d.B. & Wit, M.J.d. 2008. Comparisons between the northwestern Borborema Province, NE Brazil, and the southwestern Pharusian Dahomey Belt, SW Central Africa, in Pankhurst, R.J., et al., eds, *West Gondwana: Pre-Cenozoic Correlations Across the South Atlantic Region,* pp. 101–119, Geological Society of London. https://doi.org/10.1144/SP294.6.

Savage, M.K. 1999. Seismic anisotropy and mantle deformation: what have we learned from shear wave splitting?, *Rev. Geophys.,* **37**(1), 65–106. https://doi.org/10.1029/98RG02075

Sensarma, S., Storey, B.C. & Malviya, V.P. 2018. Gondwana Large Igneous Provinces (LIPs): distribution, diversity and significance, *Geological Society, London, Special Publications,* **463**(1), 1–16. https://doi.org/10.1144/SP463.11

Shen, W., Ritzwoller, M.H., Schulte-Pelkum, V. & Lin, F.-C. 2013. Joint inversion of surface wave dispersion and receiver functions: a Bayesian Monte-Carlo approach, *Geophys. J. Int.,* **192,** 807–836. https://doi.org/10.1093/gji/ggs050

Shi, Y., Gao, Y., Su, Y. & Wang, Q. 2012. Shear-wave splitting beneath Yunnan area of Southwest China, *Earthq. Sci.,* **25**(1), 25–34. https://doi.org/10.1007/s11589-012-0828-4

Silver, P.G. & Chan, W.W. 1991. Shear wave splitting and subcontinental mantle deformation, *J. geophys. Res.,* **96**(B10), 16429–16454. https://doi.org/10.1029/91JB00899

Svensen, H.H., Torsvik, T.H., Callegaro, S., Augland, L., Heimdal, T.H., Jerram, D.A., Planke, S. & Pereira, E. 2018. Gondwana Large Igneous Provinces: plate reconstructions, volcanic basins and sill volumes *Geol. Soc. Lond. Spec. Publ.*. **463**(1), 17–40.

Tan, P., Chen, Y., Sun, W., Li, W., Tang, G. & Cui, T. 2018. An improved H-κ-θ stacking method to determine the crustal thickness and bulk vP/vS ratios in the case of a slant Moho interface, *Chin. J. Geophys. (in Chinese),* **61**(9), 3689–3700. https://doi.org/10.6038/cjg2018M0032

Tepp, G. *et al.* 2018. Seismic anisotropy of the upper mantle below the Western Rift, East Africa, *J. geophys. Res.,* **123**(7), 5644–5660. https://doi.org/10.1029/2017JB015409

Thybo, H., Youssof, M. & Artemieva, I.M. 2019. Southern Africa crustal anisotropy reveals coupled crust-mantle evolution for over 2 billion years, *Nat. Commun.,* **10**(1), 5445, https://doi.org/10.1038/s41467-019-13267-2

Vinnik, L.P., Kosarev, G.L. & Makeyeva, L.I. 1984. Anisotropy in the lithosphere from the observations of SKS and SKKS, *Proc. Acad. Sci. USSR,* **278,** 1335–1339.

Walker, K.T., Nyblade, A.A., Klemperer, S.L., Bokelmann, G.H.R. & Owens, T.J. 2004. On the relationship between extension and anisotropy: Constraints from shear wave splitting across the East African Plateau, *J. geophys. Res.,* **109**(B8), B08302. https://doi.org/10.1029/2003JB002866

Wang, P., Huang, Z. & Wang, X. 2020. A method for estimating the crustal azimuthal anisotropy and Moho orientation simultaneously using receiver functions, *J. Geophys. Res.,* **125**(2), e2019JB018405, https://doi.org/10.1029/2019JB018405

Watanabe, M. & Oda, H. 2015. Shear-wave anisotropy of the upper and lower crusts estimated by stripping analysis of Ps-converted waves, *Tectonophysics,* **658,** 137–150. https://doi.org/10.1016/j.tecto.2015.07.016

Wessel, P., Smith, W.H.F., Scharroo, R., Luis, J. & Wobbe, F. 2013. Generic Mapping Tools: Improved version released, *Eos, Trans. Am. geophys. Un.,* **94**(45), 409–410. https://doi.org/10.1002/2013eo450001

Wüstefeld, A., Bokelmann, G., Barruol, G. & Montagner, J.-P. 2009. Identifying global seismic anisotropy patterns by correlating shear-wave splitting and surface-wave data, *Phys. Earth planet. Inter.,* **176**(3–4), 198–212. https://doi.org/10.1016/j.pepi.2009.05.006

Wüstefeld, A. & Bokelmann, G. 2007. Null detection in shear-wave splitting measurements, *Bull. seism. Soc. Am.,* **97**(4), 1204–1211. https://doi.org/10.1785/0120060190

Yuan, X., Ni, J., Kind, R., Mechie, J. & Sandvol, E. 1997. Lithospheric and upper mantle structure of southern Tibet from a seismological passive source experiment, *J. geophys. Res.,* **102**(B12), 27491−27500. https://doi.org/10.1029/97JB02379

Zang, H., Feng, M. & An, M. 2023. Evaluation and determination of anisotropic parameters using multiple shear-wave splitting analysis methods (in Chinese with English abstract), *Chinese J. Geophys.,* **66**(8), 3258–3272. https://doi.org/10.6038/cjg2022Q0363